

Effect of the Pumping-injection flow rate on Heat Transfer Characteristic of Borehole Heat Exchangers for Coupling Ground-Source Heat Pump System

Jiuchen Ma^{1,2}, Qian Jiang^{1,2,*}, Qiuli Zhang^{1,2}, Yacheng Xie^{1,2}, Yahui Wang^{1,2}, Feiyu Yi^{1,2}

* Correspondence: 596797782@qq.com¹ School of Energy Safety Engineering, Tianjin Chengjian University, Tianjin 300384, China.

Full list of author information is available at the end of the article

Abstract: A coupling ground source heat pump system (CGSHP) is established in areas where groundwater is shallow but the seepage velocity is weak, which sets up pumping and injection wells on both sides of borehole heat exchangers (BHEs). A convection-dispersion analytical model of excess temperature in aquifer that considers groundwater forced seepage and axial effects and thermal dispersion effects is proposed. A controllable forced seepage sandbox is built by equation analysis method and similarity criteria. Through indoor test and the proposed analytical model, the correctness and accuracy of the numerical simulation software FEFLOW7.1 is verified. The influence of different pumping-injection flow rate on the heat transfer characteristic of BHEs is studied by numerical simulation. The results show that the average heat efficiency coefficient of BHEs increases and the heat influence range of downstream BHEs expands with the increasing of pumping-injection flow rate. The relation curve between Pe and the increment of heat transfer rate per unit depth of BHEs ($\Delta \bar{q}$) is distributed as Gaussian function. The pumping-injection flow rate that makes Darcy velocity reaches $0.6 \times 10^{-6} \sim 1.4 \times 10^{-6} \text{ m} \cdot \text{s}^{-1}$ in the aquifer is the best reference range for CGSHP system, so $400 \sim 600 \text{ m}^3 \cdot \text{d}^{-1}$ is taken as the best pumping-injection flow rate in this paper.

Keywords: coupling ground source heat pump system; groundwater forced seepage; heat transfer; laboratory experiment; numerical simulation; analytical model

1. Introduction

Shallow geothermal resources in China are abundant but uneven. The relevant documents clearly point out that the development and utilization of shallow geothermal energy should follow the principle of adaption to local conditions (National Development and Reform Commission 2017; China Geological Survey 2018). Ground source heat pump (GSHP) system, as one of the main techniques of shallow geothermal production (Richard 2014; Richard and Marvin 2011), should take full account of local conditions in the application process. Moreover, borehole heat exchangers (BHEs) constitute a core part of the technology and the magnitude of its heat exchange quantity directly affects the efficiency of the overall unit. Therefore, it is particularly important to enhance heat transfer around BHEs.

The heat transfer performance of BHEs is studied usually by four methods, i.e., analytical method, numerical method, and in-situ thermal response test (TRT) and laboratory test. In most related fields, one or two of the above methods are adopted commonly to study the effect of natural groundwater seepage on the heat transfer performance of BHEs (A. Angelotti and L. Alberti 2014; Jinzhong 2017; Jung and Joonsang 2013; Huajun and Chengying 2009).

Numerical simulations give accurate solutions that are conducive to theoretical analysis but need extensive computational time. Hence, numerous numerical simulation softwares are

44 often applied to the research and design of BHEs, but the correctness and accuracy of these
45 softwares should be verified before (Alessandro and Rajandrea 2014; Yanling and Xiaoli 2017).
46 Angelotti et al. (A. Angelotti and L. Alberti 2014) explore the influence of groundwater
47 seepage velocity on the heat transfer characteristics of rock and soil layer by establishing a
48 single U-pipe heat transfer model through the codes MODFLOW/MT3DMS. Meanwhile, the
49 solution of numerical model is validated through the analytical solution of moving line source
50 model (MLS) on the premise that the U-pipe is simplified into an infinite line source. Hecht et
51 al. (Jozsef and Michael 2013) use FEFLOW, a finite element numerical simulation software, to
52 perform the transient heat transport simulations for the fifteen scenarios of 25 boreholes and
53 study the distribution of hydrodynamic field and temperature field in the homogeneous
54 confined aquifer. Li et al. (Chaofeng and Peter 2018) analyze the effect of unsaturated soil
55 properties and groundwater flow on the performance of GSHP system by the simulation
56 software COMSOL Multiphysics. The numerical model is validated by combining
57 experimental test results with the analytical model that takes the multiple-layer substrates and
58 groundwater flow into consideration.

59 Analytical models are preferred in most practical applications because of their excellent
60 computational time and flexibility for parameterized design. The method of moving
61 heat-source is applied in most analytical models to solve the problem of heat transfer under
62 the impact of groundwater seepage (Min and Alvin 2015). Sutton et al. (Matthew and Darin 2003)
63 and Diao et al. (Nairen and Qinyun 2004) present an analytical model considering groundwater
64 flow. They both concluded that groundwater flow could change considerably the temperature
65 distribution in the vicinity of the boreholes. Molina-Giraldo et al. (Nelson and Peter 2011)
66 evaluate the influence of thermal dispersion on temperature plumes of geothermal systems by
67 using analytical models. In the above analytical models, the axial effect is not considered and
68 the borehole is considered to be a moving infinite line heat source. Molina-Giraldo et al.
69 (Nelson and Philipp 2011) propose a moving finite line source model (MFLS) which considers
70 the combined effect of groundwater flow and axial effects but does not take the influence of
71 thermal dispersion into account. Groundwater seepage affects heat transfer by involving gross
72 heat convection and thermal dispersion, which is significant for the long-term temperature
73 response of BHEs (Jin and Joachim 2016). Therefore, an optimized analytical model, which
74 considers the thermal dispersion effect in the MFLS model, is proposed in this paper.

75 TRTs are applied to some real environments that can truly reflect the heat transfer process
76 of BHEs under the specific regional climatic characteristics and hydrogeological conditions.
77 Most TRTs are performed on a test borehole to estimate the thermo-physical properties and
78 borehole thermal resistance (Huajun and Chengying 2009; A. Michopoulos and T. Zachariadis 2013;
79 Wonjun and Ryoza 2015). From the viewpoint of model validation, the data from TRTs is not
80 suitable because TRTs' test times are short (usually 48-72 hours) and are susceptible to
81 uncontrollable factors such as weather conditions during testing (Min and Alvin 2015; David and
82 A.C 2018; Ali and Michel 2014). The indoor sandbox experiments enable to change some
83 parameters, which is conducive to improve the speed and test accuracy of the experiment
84 (Guozhu and Yimu 2016; Linlin and Lei 2015) because the experimental requirements have well
85 controllability comparing with the TRT.

86 Most studies (Selcuk and Bertrand 2018; Martin and Jonathan 2018; Junye and Gui 2017; Wenke
87 and Hongxing 2014) point out that the presence of groundwater significantly affects the heat
88 transfer between BHE and its surrounding aquifer. However, most of these study conclusions
89 are obtained under the condition of high natural seepage velocity, which is generally higher
90 than $10^{-8} \text{ m}\cdot\text{s}^{-1}$. However, many areas such as the Bohai Rim plain have abundant groundwater
91 reserves but the natural seepage velocity there is generally lower than $10^{-8} \text{ m}\cdot\text{s}^{-1}$. In this case, it
92 is usually considered that groundwater seepage has almost no effect on heat transfer of BHEs.
93 At this time, using the traditional GSHP system would render groundwater idle without

94 having the positive effect that it should have. Therefore, it is necessary to optimize the
95 traditional GSHP system for this special hydrogeological condition.

96 For the long-term application of GSHP system, the cold and heat accumulation around
97 BHEs and the heat transfer quantity of BHEs decay year-by-year, domestic and foreign
98 scholars have proposed some optimized methods and improved measures to regulate heat
99 balance of the soil. Such as, solar assisted GSHP system (Poul and Neven 2019;Giti and Younes
100 2019; H. Biglarian and M. H. Saidi 2019), and cooling tower assisted GSHP system (Zhijian and
101 Yuanwei 2018; Xuemei and Lei 2018). Giti Nouri et al. (Giti and Younes 2019) and Zhijian Liu et
102 al. (Zhijian and Yuanwei 2018) study solar assisted GSHP system and cooling tower assisted
103 GSHP system, respectively. Their research results show that the application of these hybrid
104 systems could be helpful to reach considerable savings of energy through using free resources
105 of stored heat in the ground and sun or air. However, solar-assisted GSHP system and cooling
106 tower assisted GSHP system occupy a large land area and are greatly affected by seasonal and
107 environmental factors.

108 Thus, this paper proposes a coupling ground source heat pump (CGSHP) system which
109 sets up pumping and injection wells on both sides of BHEs' well group by basing on GSHP
110 system in Tianjin, China and combining with the local special hydrogeological conditions.
111 According to CGSHP system proposed in this paper, a laboratory experiment system is
112 established and a convection-dispersion analytical model of excess temperature that considers
113 groundwater forced seepage and axial effects and thermal dispersion effects is proposed. The
114 correctness and accuracy of the numerical simulation software FEFLOW7.1 is validated with
115 the laboratory sandbox test and the proposed convection-dispersion analytical model.
116 Meanwhile, the purpose of this paper is to study the enhancement effect of heat transfer of
117 BHEs and reveal the evolution law of the temperature field and hydrodynamic field of the
118 aquifer under different pumping-injection flow rate by the numerical simulation.

119 **2. Methods**

120 Geological survey

121 China's Bohai Rim region includes the plains of the four provinces of Liaoning, Hebei,
122 Tianjin, Shandong and the surrounding mountainous areas (including the two peninsulas).
123 The Bohai Rim plain is formed in the middle Pleistocene (Q2) and the late Pleistocene (Q3) to
124 the Holocene (Q4) in the Quaternary period. The final formation of the Bohai Rim region is the
125 result of the accumulation of sediment caused by the accumulation of rivers (Rong 2012).

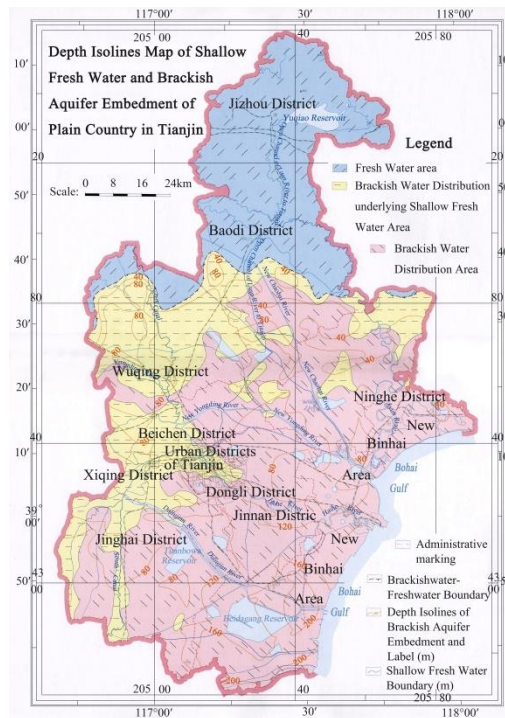


Figure 1. Depth Isolines Map of Shallow Aquifer Embedment of Plain Country in Tianjin, China

Tianjin is located in China's Bohai Rim plain, having abundant underground water and diverse hydrogeological structures. The whole Tianjin plain can be divided into the freshwater area, brackish water distribution underlying shallow freshwater area and brackish water area from north to south (Figure 1). In the structure of aquifer, the sandy layer transforms into medium coarse sand, medium sand, medium fine sand, fine sand and silty sand from north to south.

The distribution area of shallow underground brackish water in China's Binhai plain of Tianjin is 6,922 km², of which the brackish water area with a mineralization content of 2-3 g·L⁻¹ and 3-10 g·L⁻¹ are 3,753 km² and 3169 km² respectively, accounting for more than 2/3 of the city's total area (Zaiming 2012). Groundwater resources are rich in reserves and convenient for exploitation, but the hydraulic gradient and the natural seepage generally range from 1.3×10⁻² m·a⁻¹ to 12×10⁻¹ m·a⁻¹. Therefore, CGSHP system is suitable in Tianjin plain.

Underground thermo-physical properties

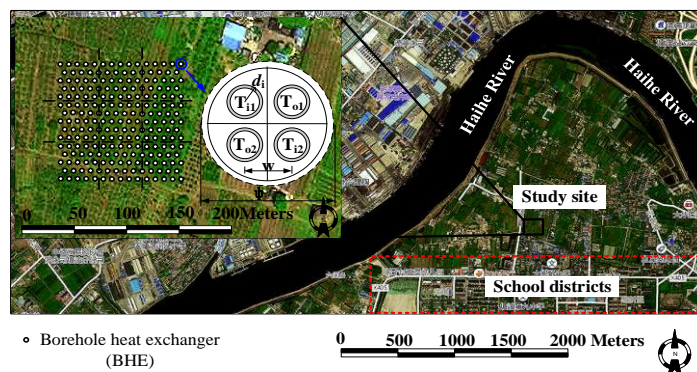


Figure 2. Location of study site in China, Tianjin, 2016 and plan view of BHEs

The GSHP system that installed in Tianjin Binhai New Area, China, 2016 is taken as the project prototype (Figure 2). The project has a research area of 150×120 m² and a vertical depth of -83m that it is divided into 5 geotechnical layers. Among whole study area, the fine sand layer has stronger permeability that is regarded as a well-developed confined aquifer, which

147 interacts with silty sand layer to form shallow-groundwater accumulation section. The
 148 geotechnical distribution and physical parameters are shown in Table 1.
 149 **Table 1.** The physical parameters of the underground rock-soil layers

soil media	Depth of distribution σ (m)	horizontal permeability k_{XY} (m ²)	porosity ε_s	volumetric heat capacity of the soil $c_s \rho_s$ (J·m ⁻³ ·K ⁻¹)	thermal conductivity λ_s (W·m ⁻¹ ·K ⁻¹)	longitudinal thermal dispersivity α_L (m)	transverse thermal dispersivity α_T (m)	Initial temperature of soil layer $T_{so}/^\circ\text{C}$
clay	0-9	5.0·10 ⁻¹⁴	0.45	2.7·10 ⁶	1.1	0.3	0.03	
silty clay	9-24	5.0·10 ⁻¹⁴	0.4	3.2·10 ⁶	1.2	0.3	0.03	
fine sand	24-44	1.2·10 ⁻¹²	0.35	1.4·10 ⁶	0.95	3.0	0.3	16
silty sand	44-80	8·10 ⁻¹³	0.38	2.4·10 ⁶	1.6	0.1	0.01	
silty clay	80-83	5.0·10 ⁻¹⁴	0.4	3.2·10 ⁶	1.2	0.3	0.03	

150 The project, which is mainly responsible for the energy supply of the adjacent school,
 151 contains 219 BHEs with a center-to-center spacing of 4-5 m. The vertical depth of the borehole
 152 is 83 m and the 2U-DN32-HDPE-BHEs with the length of 80 m is arranged in the well. The
 153 expansive soil with sand is selected as the grout materials. Water is selected as the circulating
 154 refrigerant in BHEs. The design parameters of BHEs are shown in Table 2.
 155 **Table 2.** Design Parameters of 2U-Type BHE

Parameter/Symbol (Unit)	Value
BHE depth /H (m)	80
borehole diameter / ψ (m)	0.13
outer diameter of branch pipe-in(out)/ $d_{i(o)}$ (m)	0.032
wall thickness of branch pipe-in(out)/ $b_{i(o)}$ (m)	0.0029
adjacent branch pipe distance / w (m)	0.05
thermal conductivity of pipe-in(out) material/ $\lambda_{pi(o)}$	0.6
thermal conductivity of refrigerant (water)/ λ_r	0.65
volumetric heat capacity of refrigerant (water) / $c_r \rho_r$	4.18·10 ⁶
volumetric heat capacity of grout/ $c_g \rho_g$ (J·(m ⁻³ ·K ⁻¹))	2.19·10 ⁶
thermal conductivity of grout/ λ_g (W·m ⁻¹ ·K ⁻¹)	1.9

156 Heat-seepage coupling model

157 It is assumed that the seepage process of aquifer satisfies the following conditions: the
 158 physical parameters of aquifer and groundwater do not change with temperature; the seepage
 159 direction of groundwater is single and the vertical seepage process is ignored. According to
 160 the continuity equation of seepage flow and Darcy law (Yujin and Ryoza 2008), the continuity
 161 governing equation (1) and momentum governing equation (2) in the anisotropic and
 162 homogeneous aquifers are established:

$$163 \quad [\varepsilon_s \gamma_f + (1 - \varepsilon_s) \gamma_s] \frac{\partial h}{\partial t} + \nabla \cdot u_f = Q_p \quad (1)$$

$$164 \quad u_f = - \frac{k \rho_f g}{\mu_f} \frac{\partial h}{\partial x} \quad (2)$$

165 In order to describe the change of heat transfer characteristics of BHEs in the aquifer
 166 under complex space-time conditions accurately on the basis of the convective-conduction
 167 equation (Antonio and Michele 2013), the control equation of three-dimensional unsteady
 168 convective - thermal dispersion is established by taking the thermal dispersion effect into
 169 account.

$$[\varepsilon_s \rho_f c_f + (1 - \varepsilon_s) \rho_s c_s] \frac{\partial T}{\partial t} = -\rho_f c_f u_f \nabla \cdot T + \nabla \cdot [(\Lambda^{\text{cond}} + \Lambda^{\text{disp}}) \nabla \cdot T] + Q_T \quad (3)$$

In which, the conductive part of thermodispersion tensor Λ^{cond} and the dispersive part of thermodispersion tensor Λ^{disp} are determined by equation (4) and (5) respectively.

$$\Lambda^{\text{cond}} = [\varepsilon_s \lambda_f + (1 - \varepsilon_s) \lambda_s] \delta_{ij} \quad (4)$$

$$\Lambda^{\text{disp}} = \rho_f c_f \left(\alpha_T u_f \delta_{ij} + (\alpha_L - \alpha_T) \frac{u_i u_j}{u_f} \right) \quad (5)$$

The problem for determining solution of seepage flow is associated with the problem of heat transfer by the momentum equation (2), so the heat-seepage coupling model is constructed in the aquifer. The discharge (suction) heat process of the borehole can be considered as the source (sink) term in the aquifer thermal migration model. Because the diameter of the vertical borehole is much smaller than its depth, in order to consider effectively the influence of groundwater seepage on the heat transfer of BHE, the heat transfer process of BHE is simplified to the heat transfer process of the moving finite line heat source in the semi-infinite medium.

On the basis of considering the thermal dispersion effect and the spatial position of BHE, the moving finite line heat source model (MFLS) (A. Michopoulos; T. Zachariadis 2013) is improved. Under the premise of constant heat flow rate per unit length of BHE, the optimized analytical model (Eq.6-7) is obtained by applying the method of images and the moving source theory. The optimized analytical model takes into account the heat convection, heat conduction and thermal dispersion effects in the process of groundwater seepage to determine the transient temperature in the aquifer caused by heat from the heat exchanger and is coupled with the internal heat transfer process of the borehole.

$$\Delta T(x, y, z, t) = \frac{q}{2\pi \sqrt{\lambda_x \lambda_y}} \exp \left[\frac{\rho_f c_f u_f (x - x')}{2\lambda_x} \right] \left[\int_0^H f(x, y, z, t) dz - \int_{-H}^0 f(x, y, z, t) dz \right] \quad (6)$$

$$f(x, y, z, t) = \frac{1}{4\sqrt{(x-x')^2 + (y-y')^2 + (z-z')^2}} \left[\exp \left(-\frac{\rho_f c_f u_f \sqrt{\frac{(x-x')^2}{\lambda_x \lambda_x} + \frac{(y-y')^2}{\lambda_x \lambda_y} + \frac{(z-z')^2}{\lambda_x \lambda_e}}}{2} \right) \operatorname{erfc} \left(\frac{\sqrt{\frac{(x-x')^2}{\lambda_x \lambda_x} + \frac{(y-y')^2}{\lambda_x \lambda_y} + \frac{(z-z')^2}{\lambda_x \lambda_e}} \rho_e c_e - \frac{\rho_f c_f u_f t}{\lambda_x}}{2\sqrt{\frac{\rho_e c_e}{\lambda_e} t}} \right) + \exp \left(-\frac{\rho_f c_f u_f \sqrt{\frac{(x-x')^2}{\lambda_x \lambda_x} + \frac{(y-y')^2}{\lambda_x \lambda_y} + \frac{(z-z')^2}{\lambda_x \lambda_e}}}{2} \right) \operatorname{erfc} \left(\frac{\sqrt{\frac{(x-x')^2}{\lambda_x \lambda_x} + \frac{(y-y')^2}{\lambda_x \lambda_y} + \frac{(z-z')^2}{\lambda_x \lambda_e}} \rho_e c_e + \frac{\rho_f c_f u_f t}{\lambda_x}}{2\sqrt{\frac{\rho_e c_e}{\lambda_e} t}} \right) \right] \quad (7)$$

In the analytic model, $\rho_e c_e$ is the volumetric heat capacity of the porous medium (Eq.8). When the thermal conductivity in the aquifers is the same in each direction, the thermal conductivity components of the Λ^{cond} are determined by equation (9). λ_x and λ_y is the effective longitudinal and transverse thermal conductivity coefficient, respectively, which are determined by Eq.10 and Eq.11. r is the distance to the source located on the z -axis at the (x_0, y_0, z') coordinates (Eq.12).

$$\rho_e c_e = \varepsilon_s \rho_f c_f + (1 - \varepsilon_s) \rho_s c_s \quad (8)$$

$$\lambda_x^{\text{cond}} = \lambda_y^{\text{cond}} = \lambda_z^{\text{cond}} = \lambda_e = \varepsilon_s \lambda_f + (1 - \varepsilon_s) \lambda_s \quad (9)$$

$$\lambda_x = \lambda_e + \alpha_L u_f \rho_f c_f \quad (10)$$

$$\lambda_y = \lambda_e + \alpha_T u_f \rho_f c_f \quad (11)$$

$$r = \sqrt{(x-x_0)^2 + (y-y_0)^2 + (z-z')^2} \quad (12)$$

When the thermal dispersion effect in the aquifer is ignored ($\lambda_x=\lambda_y=\lambda_e$), the excess temperature analysis model (Eq.6) and (Eq.7) can be simplified to Eq. 13 and Eq.14.

$$\Delta T(x, y, z, t) = \frac{q}{2\pi\lambda_e} \exp\left[\frac{\rho_f c_f u_f (x-x')}{2\lambda_e}\right] \left[\int_0^H f'(x, y, z, t) dz' - \int_{-H}^0 f'(x, y, z, t) dz' \right] \quad (13)$$

$$f'(x, y, z, t) = \exp\left(-\frac{\rho_f c_f u_f r}{2\lambda_e}\right) \operatorname{erfc}\left(\frac{r\rho_e c_e - \rho_f c_f u_f t}{2\sqrt{\rho_e c_e \lambda_e t}}\right) + \exp\left(\frac{\rho_f c_f u_f r}{2\lambda_e}\right) \operatorname{erfc}\left(\frac{r\rho_e c_e + \rho_f c_f u_f t}{2\sqrt{\rho_e c_e \lambda_e t}}\right) \quad (14)$$

3.Experimental System

In order to ensure the reasonable use of the limited laboratory indoor space, the fine sand layer, which was a typical hydrogeological medium in shallow the aquifer, with the area of $20 \times 16 \text{m}^2$ and the buried depth of 24~44m in Figure 2 were selected as the engineering prototype for designing and building a complete laboratory experimental system. The engineering prototype contained 6 ordinals arranged BHEs with the tube pitch of 4m.

Design and Construction of Experimental system

The experimental system consists of a sandbox, a heating apparatus, a flow conditioning apparatus and a data-acquisition apparatus (Figure 3). Since the seepage and heat transfer processes in the seepage sandbox and the engineering prototype followed the same form of governing equations (Eq.1-3), the similitude relation ratio of basic design parameters was determined by equation analysis method according to the principle of similarity criteria (Min and Alvin 2015; X. Mao and H. Prommer 2006).

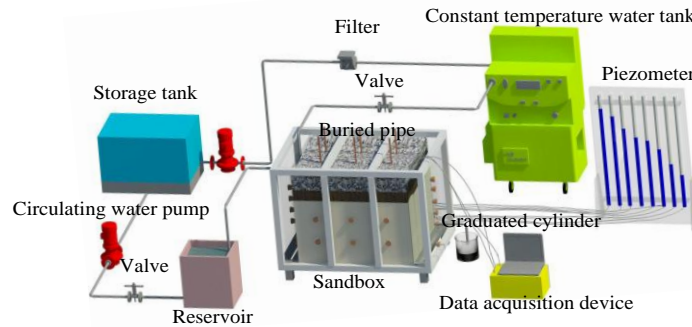


Figure 3. Schematic diagram of the experimental system

The proportional relationship between hydrogeology and thermophysical parameters of aquifers was 1:1 due to the use of equal volumetric weight filling of raw sand and seepage of raw water. In order to shorten the experimental period, the proportional relationship between the heat intensity of BHEs and the difference of water head was set as 1:1. The geometric size proportional relationship between the actual and experimental was determined as 20:1. The Pr (Eq.15), Fo (Eq.16) and Pe (Eq.17) in the engineering prototype and the sandbox were required to be equal in order to ensure that the experimental system can reproduce effectively the heat-seepage migration process of the aquifer. Thus, the operation time proportional relationship between the actual and the experimental was determined to be 400:1 and the seepage velocity proportional relationship between the actual and the experimental was determined to be 1:20, so as to determine other design parameters, as shown in Table 3.

$$Pr = \frac{\rho_f \rho_e c_e}{\mu_f \lambda_e} = \frac{\rho_{fm} \rho_{em} c_{em}}{\mu_{fm} \lambda_{em}} = Pr_m \quad (15)$$

$$Fo = \frac{\lambda_e t}{\rho_e c_e l^2} = \frac{\lambda_{em} t_m}{\rho_{em} c_{em} l_m^2} = Fo_m \quad (16)$$

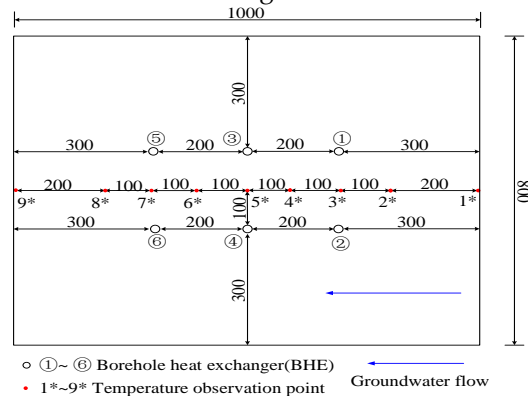
$$Pe = \frac{\rho_f c_f u l}{\lambda_e} = \frac{\rho_{fm} c_{fm} u_m l_m}{\lambda_{em}} = Pe_m \quad (17)$$

240 **Table 3.** Engineering prototype and experimental system design parameters

classify	volume $x \cdot y \cdot z$ (m^3)	pressure diaphragm thickness σ (m)	confined		heat transfer rates per unit borehole depth q ($W \cdot m^{-1}$)	Darcy velocity u_i ($m \cdot s^{-1}$)	operatio n time t
			aquifer (fine sand layer) thickness ω (m)	tube pitch l (m)			
prototype	20×16×20	4	12	4	50	1.2×10^{-7}	90d
test-bed	1.0×0.8×1	0.2	0.6	0.2	50	2.4×10^{-6}	5.4h

241 According to the geometric similarity ratio, the sandbox was set to $1.2 \times 0.8 \times 1.2 m^3$ while
 242 the seepage region was $1 \times 0.8 \times 1 m^3$ and the confined aquifuge region was $1 \times 0.8 \times 0.2 m^3$. The
 243 liquid supply/discharge region was $0.1 \times 0.8 \times 1.2 m^3$, which was symmetrically set at both
 244 ends. Then five overflow holes ($\Phi 20$ mm) with spacing of 0.2m were drilled in the centerline
 245 of plexiglas's plate on the outsides of the liquid supply/discharge region. During the
 246 experiment, rubber plugs of overflow holes at different heights were opened to control the
 247 hydraulic difference between the liquid supply/drainage region, so as to change the seepage
 248 velocity in the seepage region. Plexiglas's plate with the equally distributed holes ($\Phi 5$ mm)
 249 was installed between liquid supply/discharge region and the seepage area to ensure that the
 250 seepage solution flows horizontally and evenly in the aquifer.

251 The K-type ($\pm 0.1^\circ C$) thermocouple treated with waterproof and anti-corrosion package
 252 was selected to measure aquifer temperature. Nine K-type thermocouples were embedded
 253 0.5m away from the bottom of the sandbox. The data acquisition apparatus was used to
 254 record temperatures of the aquifer. Then, six PPR pipes with 1.5m-long, which fixed on the
 255 bottom plate of the sandbox, were wound evenly with electric heating wire (50W/m) to
 256 simulate the BHEs as the heat source device of the sandbox. The plane layout of BHEs and
 257 temperature observation points was shown as Figure 4.



258
 259 **Figure 4.** Layout of BHEs and temperature observation points (unit: mm)

260 The precision bath circulator THD-3015 was selected as the cold/heat source equipment
 261 in order to ensure that the temperature of the circulating groundwater meets the
 262 requirements of the test. Furthermore, the thermal insulation materials with the thickness of
 263 0.15 m were attached to the outside of the sandbox device, connecting pipes, storage tank and
 264 reservoir. After pasting thermal insulation materials, six K-type thermocouples were fixed
 265 respectively on all six sides of the sandbox to measure the heat loss of the experimental
 266 system.

267 *Experimental scheme*

268 The sand sample and the groundwater were collected in the aquifer at the underground
 269 depth of 24-44m in the relevant project. The sandbox was filled with equal volumetric weight
 270 by layered wet filling method. Each raw sand layer with a thickness of 50mm was filled while
 271 the raw underground water was sprayed evenly and the sand layer was compacted to ensure
 272 that the porous medium in the sandbox has unit weight of $1.68\pm 0.1 \text{ kg}\cdot\text{L}^{-1}$, which was similar
 273 to that of the underground aquifer. The filling height of raw sand was 1m, and then the upper
 274 part of the sandbox was laid with a 0.2m clay-gravel layer as the confined aquifuge to isolate
 275 the aquifer from the external environment. The photograph of the sandbox without the
 276 thermal insulation material was shown as Figure 5.



277
 278 **Figure 5.** Photograph of the infiltration sandbox

279 After the establishment of the experimental system, the room temperature was first
 280 maintained at 18°C by central air conditioning, and then the 16°C underground raw water
 281 was filled into the sandbox for the exhaust gas process of porous media. When all
 282 temperature observation points in the sandbox were maintained at $16\pm 0.1^{\circ}\text{C}$, and the water
 283 level in the piezometer was stable and no bubbles appeared, the porous medium of the
 284 sandbox could be considered as saturated aquifer.

285 Before the experiment, it was proved that Darcy velocity was $2.4\pm 0.02\times 10^{-6}$ ($Pe\approx 2.5$) when
 286 the hydraulic difference was 0.2m, which satisfied the proportional relationship between
 287 actual and experimental seepage velocity 1:20. During the experiment, the 16°C underground
 288 raw water with 0.2 m hydraulic difference was filled continuously into the sandbox to ensure
 289 a stable Darcy velocity, simultaneously, BHEs ① ~ ④ were opened in the test. The
 290 experimental run time was set at 5.4 h and the temperature of each observation point was
 291 recorded per 1 min. Through the experiment, it was found that the temperature measurement
 292 range of the six thermocouples outside the thermal insulation sandbox was $18\pm 0.5^{\circ}\text{C}$, so the
 293 heat loss from the sandbox was in negligible level.

294 **4. Numerical model**

295 *Compared with analytical and experimental data*

296 According to the engineering prototype, FEFLOW 7.1 is used to establish the geometric
 297 model, mesh division (triangular element non-equidistant) and set the parameters, and then
 298 perform numerical simulation calculations. Meanwhile, MATLAB 2012 is used to calculate
 299 the transient temperature response caused by the running BHE in engineering prototype,
 300 according to the unsteady analytical model of the excess temperature in the aquifer (Eq.6-7).
 301 Then, the experimental result and the analytical solution of the engineering prototype are
 302 compared with the numerical solution of the engineering prototype.

303 In the numerical simulation, the clay layer is defined as a confined aquifuge while the
 304 fine sand layer with a thickness of 20m exists as a confined aquifer. The clay layer in the

305 upper part of the study area is defined as the impervious and adiabatic boundary while the
 306 external environmental impact is ignored. Moreover, the four flanks of the 20×16×83 m³
 307 model are defined as the fixed hydraulic head and constant temperature boundary. Then, the
 308 parameters of the six ordinals arranged BHEs in this area are set according to Table 2. In
 309 addition, the triangular element non-equidistant mesh generation is adopted in the entire
 310 geotechnical layer. The physical model has a total number of nodes of 51740 and a grid
 311 number of 93156. The fixed-time step method is used in the solution process. The total
 312 number of time steps is 324 when the time-step length is set to 1 min and the maximum
 313 iteration is 2500 times per step.

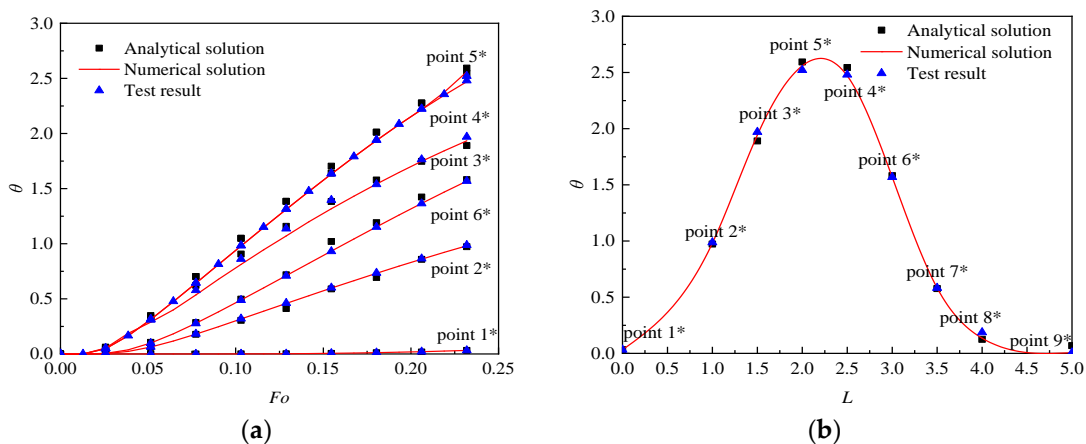
314 For facilitating the comparison, the time t , the excess temperature ΔT and the coordinate
 315 displacement x are all in a dimensionless form. Due to the different proportional relationship
 316 between the engineering prototype and the experimental system in operation time and
 317 geometric size, Fo is taken as dimensionless time (Eq.16), θ is taken as dimensionless excess
 318 temperature (Eq.18) and L is taken as dimensionless coordinate displacement (Eq.19).
 319 Meanwhile, the root mean square error (RMSE) of dimensionless excess temperature θ (Eq.20)
 320 is selected as the similarity index between experimental results, analytical solutions and
 321 numerical solutions.

$$322 \quad \theta = \frac{4\pi\lambda_c\Delta T}{q} \quad (18)$$

$$323 \quad L = \frac{x}{l} \quad (19)$$

$$324 \quad \text{RMSE} = \sqrt{\frac{\sum_{i=1}^n (\theta_{N(i)/A(i)} - \theta_{E(i)})^2}{n}} \quad (20)$$

325 in which $\theta_{N(i)/A(i)}$ corresponds to the numerical solutions and analytical solutions respectively,
 326 and $\theta_{E(i)}$ corresponds to the experimental result.



327 **Figure 6.** Comparison of multi-tube (Four-tube) analytical solution and numerical solution with
 328 experimental result($y=0m, z=0.5m$): (a) temperature response θ over Fo (the observation points 1*~6*); (b)
 329 temperature response θ over dimensionless distance L ($Fo=0.232$)

330 The RMSE between the analytical solutions and the experimental results in Figure 6(a)
 331 does not exceed 5% while the RMSE between the numerical solution and the experimental
 332 result does not exceed 1%. Besides, the RMSE between the analytical solution and the
 333 experimental result is 3.8% and the RMSE of the numerical solutions and experimental results
 334 is 0.5% in Figure 6(b). The results show that the analytical solution and experimental results
 335 are consistent with the numerical solution, so FEFLOE 7.1 can simulate effectively and
 336 accurately the heat transfer process of BHEs in the aquifer.

337 *Compared with existing studied data*

338 The numerical solutions regarding the mean temperature change of the aquifer are then
 339 compared to available data derived from (Jozsef and Michael 2013). Since the studies in
 340 literature refer to different ground properties and groundwater velocities, as well as to
 341 different dimensions, the comparison is performed by calculating for each condition in the
 342 papers the Pe , Fo , $\bar{\theta}$.

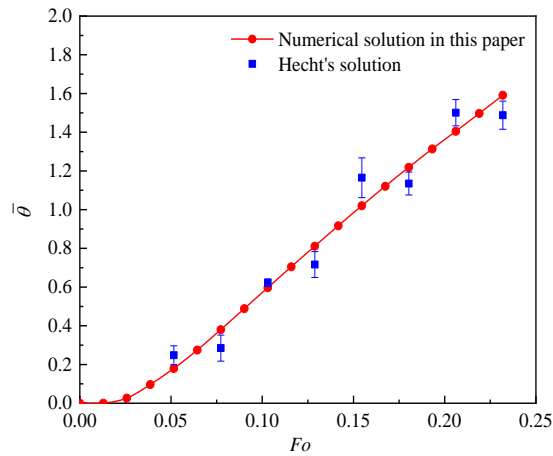


Figure 7. Comparison of multi-tube (Four-tube) numerical solution with Hecht's solution (Jozsef and Michael 2013): dimensionless mean temperature ($\bar{\theta} = 4\pi\lambda_e\Delta T/q$) change over Fo

Table 4. Comparison between the numerical solutions and the Hecht's solution in: $\bar{\theta}$ and relative error for Fo

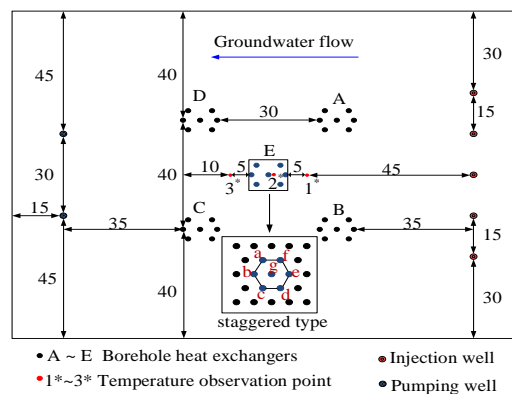
Fo	$\bar{\theta}$	Fit standard	$\bar{\theta}$ relative
		mean deviation	error (%)
0.05153	0.17937	0.248	4.9%
0.07729	0.37967	0.2846	-6.7%
0.10306	0.59666	0.62288	1.9%
0.12882	0.81075	0.7164	-6.7%
0.15459	1.01956	1.165	10.3%
0.18035	1.21858	1.1348	-5.9%
0.20612	1.40478	1.5009	6.8%
0.23188	1.59073	1.48792	-7.3%

343 After comparing Pe , it is found that the “scenario 12” in Hecht's research (Jozsef and
 344 Michael 2013) are close to the working conditions in this paper (Figure 7). The results show
 345 that the maximum error is 10.3% and the other errors are less than 10%. Therefore, using
 346 FEFLOW7.1 to simulate the heat transfer process of the BHEs under forced seepage is
 347 effective and correct.

348 5. Results and Discussion

349 This section explores the influence of the pumping-injection flow rate of CGSHP system
 350 compared with the established traditional GSHP system (Figure 2) on enhancing the heat
 351 transfer effect.

352 Generalized model and Operation scheme



353

354 **Figure 8.** Geometric arrangement of BHEs and pumping - injection wells (unit: m)

355 Because of the complex and diverse layout of the on-site well group and a large number
 356 of boreholes, the BHEs (Figure 2) are generalized into five groups of BHEs in Figure 8. For
 357 each group, there are seven boreholes arranged according to a staggered layout while the
 358 space between each borehole is 4-5 m. To ensure the groundwater synchronous recharge, two
 359 pumping wells and five injection wells are set up. Moreover, the design parameters of BHE
 360 are shown in Table 2. The seven working wells are all incomplete diving wells with a depth of
 361 60 m and a diameter of 0.4 m. Meanwhile, the filter is placed at a depth of 40-50 m.

362 On the grounds of the layout of the well group, the horizontal calculation area is 150×120
 363 m² and the vertical calculation range is 0~83 m. From the top to the bottom, the rock-soil
 364 layer with a thickness of 83 m is separated into five types of horizontal fault. The spatial
 365 distribution and physical properties of that layer are shown in Table 1.

366 In the numerical calculation, the silty clay layer in the upper and lower part of the study
 367 area is defined as the impervious and adiabatic boundary as the effects of atmospheric
 368 rainfall and evaporation are ignored. The four flanks of the physical model are defined as the
 369 fixed hydraulic head and constant temperature boundary. In addition, the pumping-injection
 370 wells are defined as the constant flow boundary. The triangular element non-equidistant
 371 mesh division is adopted for each rock-soil layer. Local refinement of the mesh is set in the
 372 location of BHEs and the pumping-injection wells.

373 The number of total nodes and grid in the physical model is 248,752 and 413,295. The
 374 fixed-time step method is used in the solution process. The time step, the total time step and
 375 the maximum iteration are set to 1d, 3650 and 2500(times per step) respectively. Based on the
 376 established model, the simulation calculations are carried out for eight kinds of operation
 377 modes respectively (Table 5).

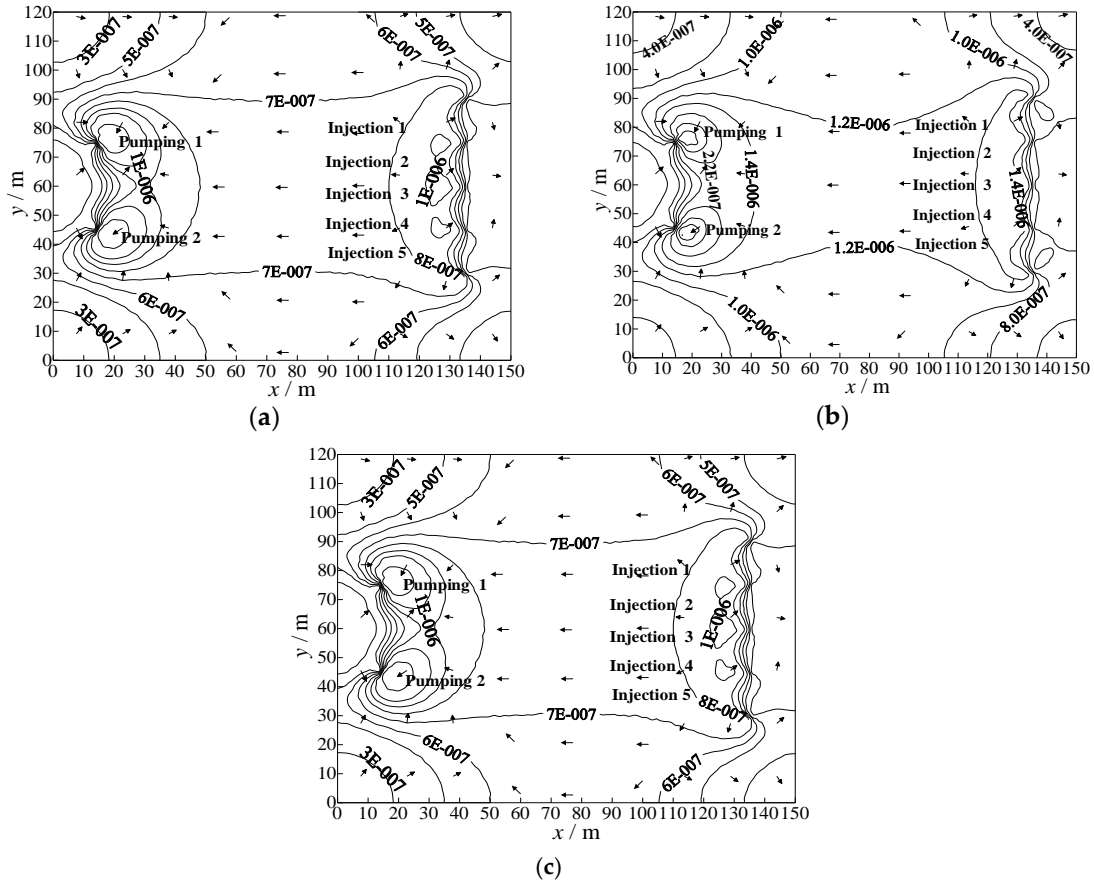
378 **Table 5.** Operation scenarios of the coupling pumping-injection wells and BHEs

Scenario	Total flow rate of refrigerant per borehole (m ³ ·d ⁻¹)	Pumping quantity of single well (m ³ ·d ⁻¹)	Rated power of the submersible pump kW	Recharge quantity of single well (m ³ ·d ⁻¹)	Rated power of the pressure pump kW
1	30	0	0	0	0
2	30	100	1.5	40	0.75
3	30	200	2.2	80	1.1
4	30	300	4	120	2.2
5	30	400	5.5	160	2.2
6	30	500	5.5	200	3
7	30	600	7.5	240	3
8	30	700	7.5	280	3

379 To divide one operation cycle (1 year) into four stages that are followed by summer
 380 cooling stage (4 months), autumn intermittent stage 1 (2 months), winter heating stage (4
 381 months) and spring intermittent stage 2 (2 months). The system runs five operation cycles
 382 and BHEs operate continuously for 10 hours per day in both the cooling and heating stage.
 383 The inlet water temperature of BHEs during cooling/heating stage is constant at 31 °C /6 °C is
 384 respectively.

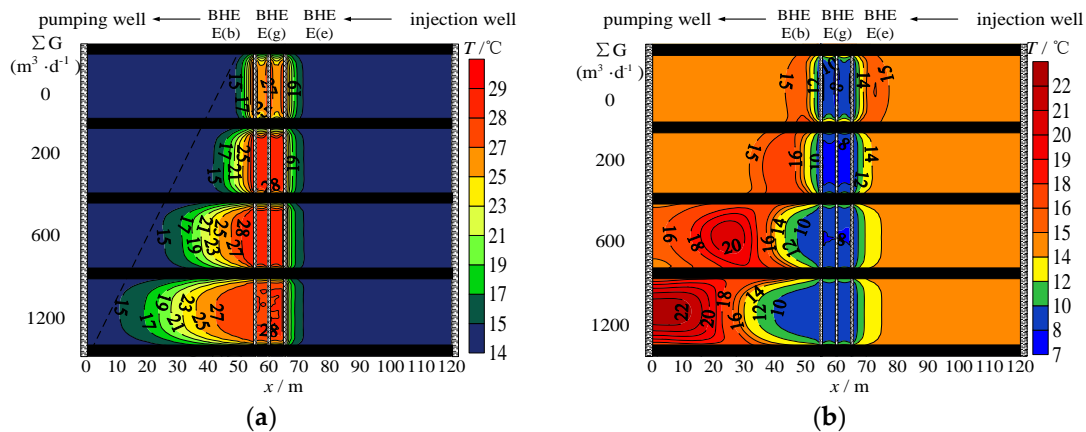
385 *Analysis and discussion*

386 The Darcy velocity and the hydrodynamic distribution have a significant difference in
 387 the same aquifer since the total pumping-injection flow rate (ΣG) is different (Figure 9). Darcy
 388 velocity, which increases approximately 10 time, increases from $2.4 \sim 3.2 \times 10^{-7} \text{ m}\cdot\text{s}^{-1}$ to
 389 $2.0 \sim 3.0 \times 10^{-6} \text{ m}\cdot\text{s}^{-1}$ When the total pumping-injection flow rate increases from $200 \text{ m}^3\cdot\text{d}^{-1}$ to 1200
 390 $\text{m}^3\cdot\text{d}^{-1}$.



391 **Figure 9.** Spatial hydrodynamic distribution in the fine sand layer on the 120d under the different total
 392 pumping-injection flow rate ΣG : (a) $\Sigma G=200 \text{ m}^3\cdot\text{d}^{-1}$; (b) $\Sigma G=600 \text{ m}^3\cdot\text{d}^{-1}$; (c) $\Sigma G=1200 \text{ m}^3\cdot\text{d}^{-1}$

393 Due to the difference of pumping-injection flow rate, profile temperature fields have a
 394 significant difference in the same aquifer (Figure 10). Taking BHEs' well group E as the
 395 research object, the injection well and the pumping well with a spacing of 120 m are defined
 396 as the upstream and downstream boundaries, respectively.

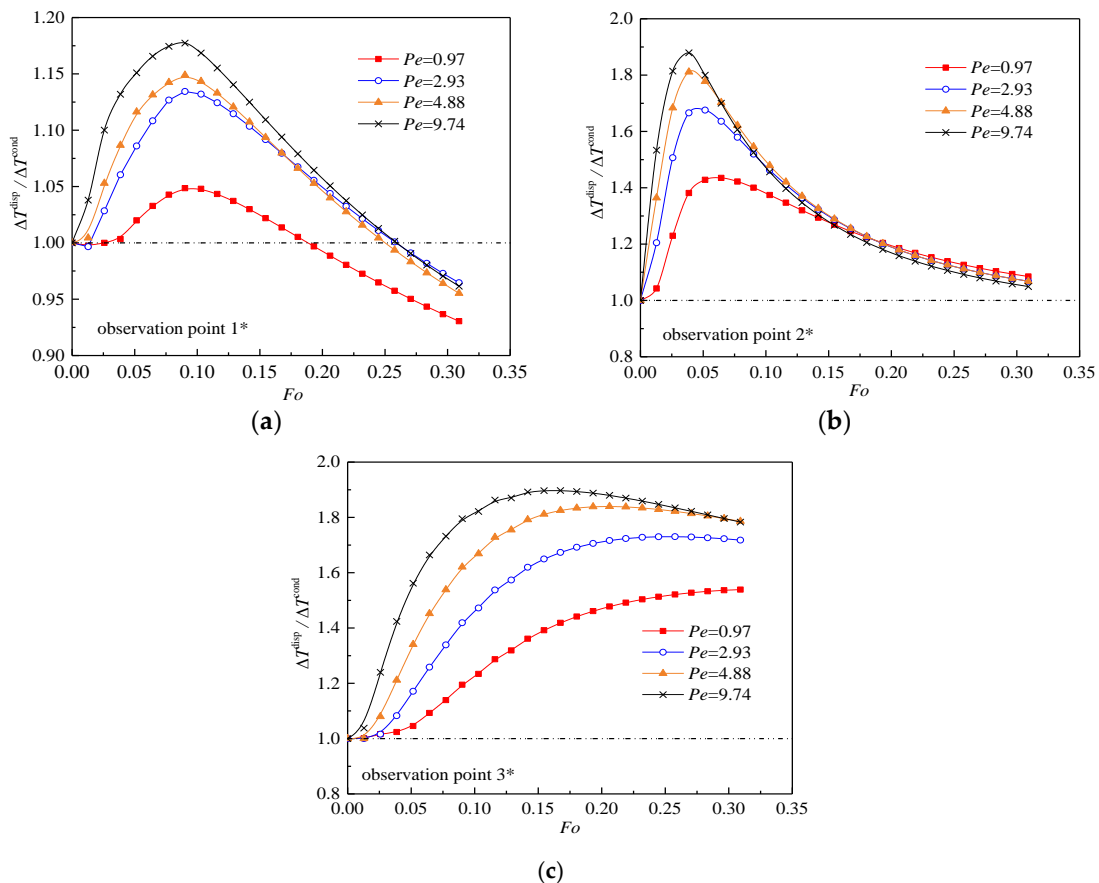


397 **Figure 10.** Profile temperature field in the fine sand aquifer under the different total pumping-injection
 398 flow rate: (a) the end of the cooling stage (120 d); (b) the end of the heating stage (300 d)

399 To describe accurately the evolution process of the aquifer's temperature field under
 400 different operation modes, the calculation area with a temperature change of $\pm 0.5\text{ }^{\circ}\text{C}$ is
 401 defined as the thermal diffusion range of the BHEs. Besides, the heat-influencing radius is
 402 defined as the coordinate distance between E (g) and the farthest acting position.

403 When the pumping-injection flow rate is $0\text{ m}^3\cdot\text{d}^{-1}$, there is only the heat conduction
 404 between BHEs and the aquifer as well as between the aqueous medium units. The heat
 405 transfer process is slow and the heat influence range is diffused symmetrically around BHEs.
 406 By the end of the cooling stage (120d), the thermal radius of BHEs in both upstream and
 407 downstream areas is 11 m.

408 The range of thermal diffusion in the downstream area of BHEs significantly expands
 409 with the pumping-injection flow rate increases from $200\text{ m}^3\cdot\text{d}^{-1}$ to $1200\text{ m}^3\cdot\text{d}^{-1}$. At the 120 d, the
 410 thermal radius along the direction of pumping reaches 19 m, 35 m and 49 m, so the thermal
 411 radius of $1200\text{ m}^3\cdot\text{d}^{-1}$ is 2.6 times of that of $200\text{ m}^3\cdot\text{d}^{-1}$. With the increase of the flow rate, the
 412 migration speed of the temperature fronts accelerates and the thermal radius enlarges
 413 continuously, moreover, the thermal radius in the upstream zone is smaller than 11m.



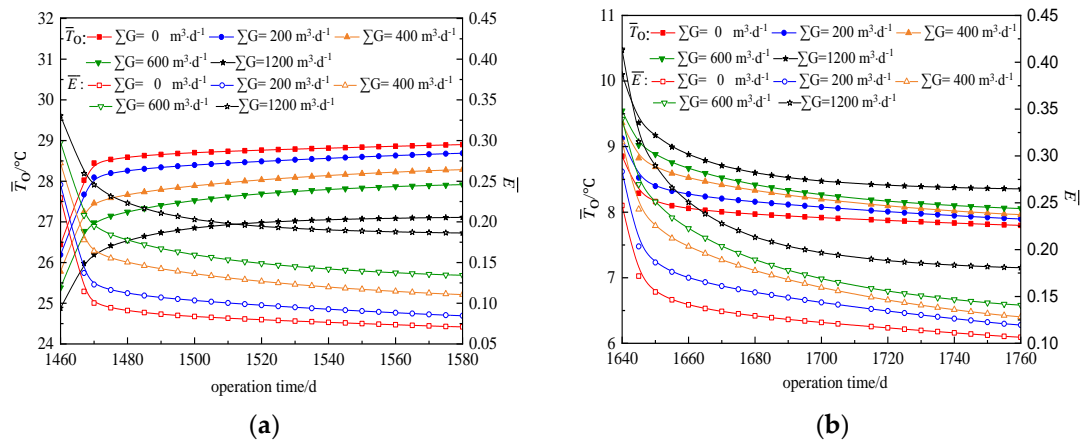
414 **Figure 11.** Temperature response dynamic curve in the fine sand aquifer at the first cooling stage: (a) the
 415 upstream area of BHEs (the observation point 1*); (b) the inside area of BHEs (the observation point 2*);
 416 (c) the downstream area of BHEs (the observation point 3*)

417 According to the theory of heat and mass transfer, it is precisely because of the increase
 418 of Darcy velocity that the convective heat transfer intensity and thermomechanical dispersion
 419 effect are improved correspondingly, thereby expanding the range of thermal diffusion in the

420 downstream region and alleviating the thermal accumulation phenomenon of BHE. So, in
 421 order to obtain the difference between the temperature response ΔT^{disp} with forced
 422 groundwater seepage and the temperature response ΔT^{cond} without groundwater seepage at
 423 different temperature observation points, the dynamic variation of $\Delta T^{\text{disp}}/\Delta T^{\text{cond}}$ with time is
 424 calculated (Figure 11).

425 As shown in Figure 11 (a), the mutative extent of temperature decreases gradually with the
 426 running time. When the running time exceeds 50% of the whole period ($Fo \geq 0.2$), $\Delta T^{\text{disp}}/\Delta T^{\text{cond}} < 1$. As
 427 shown in Figure 11 (b), $\Delta T^{\text{disp}}/\Delta T^{\text{cond}}$ tends to be stable gradually with time. At the end of the cooling
 428 stage(120d), $\Delta T^{\text{disp}}/\Delta T^{\text{cond}} > 1$. The change of Darcy velocity has no obvious influence on the change
 429 rate and amplitude of excess temperature because the thermal convection and thermal dispersion
 430 enhances thermal interference between BHEs. As shown in Figure 11 (c), with the passage of time, the
 431 excess temperature tends to be stable and the curve of $\Delta T^{\text{disp}}/\Delta T^{\text{cond}}$ tends to be smooth. The mutative
 432 degree of excess temperature enhances with the increase of Darcy velocity but the difference between
 433 ΔT^{cond} and ΔT^{disp} tends to decrease when Darcy velocity increases to a certain extent.

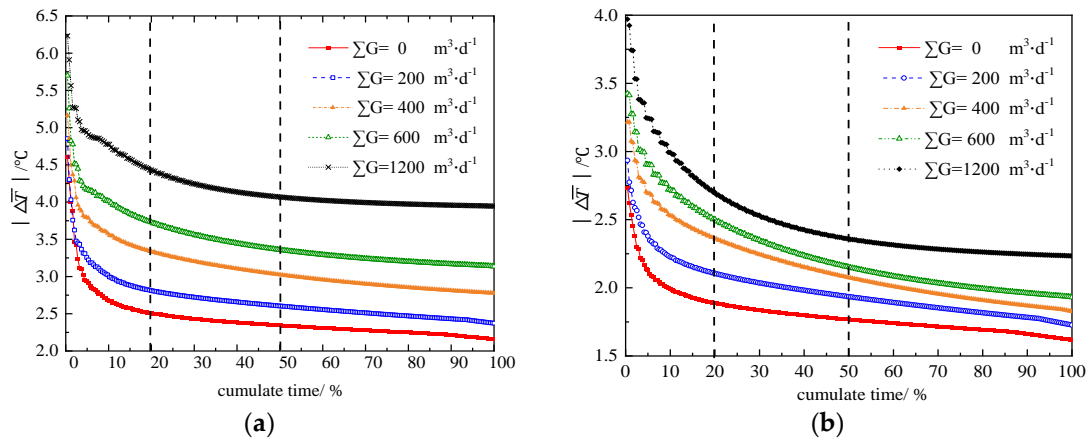
434



435 **Figure 12.** Dynamic changes of the average outlet water temperature (\bar{T}_o) and the average heat transfer
 436 efficiency ($\bar{E} = \bar{Q}/\bar{Q}' = |\bar{T}_i - \bar{T}_o|/|\bar{T}_i - \bar{T}_{so}|$) of BHEs in the fifth operation cycle: (a) the cooling stage; (b)
 437 the heating stage

438 At the early stage of various operation modes, due to the large temperature difference in
 439 heat transfer between the boreholes and the rock-soil layer, the temperature difference
 440 between the inlet with outlet water of BHEs is higher and the corresponding energy efficiency
 441 coefficient also rise, (Figure 12). The heat exchange rate reduces because of the decreasing
 442 temperature difference between the boreholes and the surrounding medium. As a result, the
 443 temperature difference of the inlet and outlet water of BHEs decreases rapidly. At the end of
 444 the fifth operation cycle, the average heat transfer efficiency of the five types of operation
 445 modes in the cooling stage is 7.1%, 8.5%, 11.1%, 13.4% and 18.6% while the average heat
 446 transfer efficiency in the heating stage is 10.6%, 11.9%, 12.8%, 14.6% and 18.1% respectively.

447

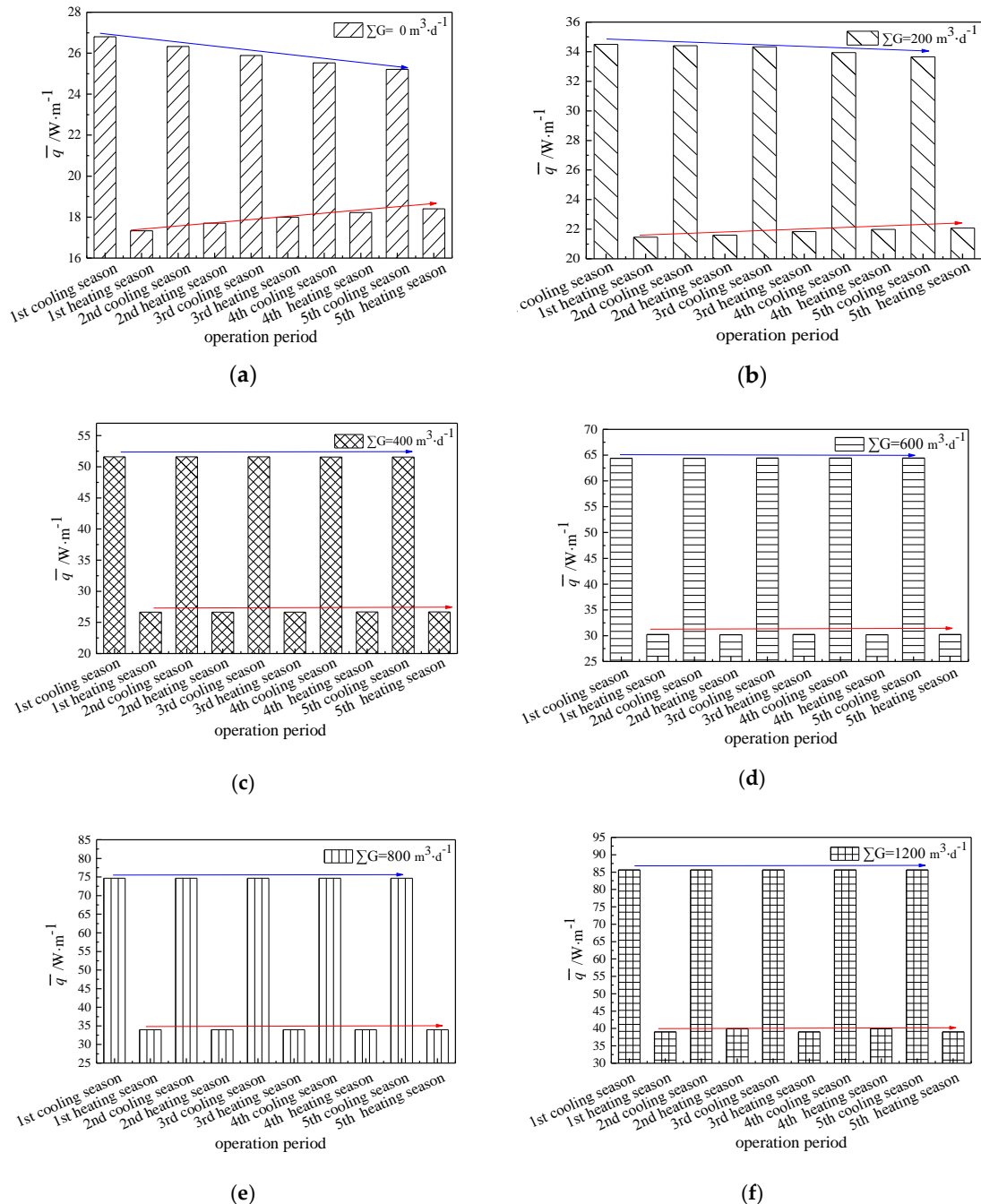


448 **Figure 13.** Cumulative distributions of the temperature difference of the inlet and outlet water of BHEs:
 449 (a) the cooling stage; (b) the heating stage

450 The cumulative distribution curve can be used as another evaluation index to describe
 451 the duration of a certain heat exchange efficiency of BHEs (Figure 13). The absolute values of
 452 the inlet and outlet temperature difference of BHEs is arranged in descending order, and the
 453 cumulative average temperature difference distribution in the cooling stages and heating
 454 stages over the whole simulation stages (5 years) is calculated. When the cumulate time
 455 exceeds 20% of the total operation stage, the temperature difference tends to be moderate,
 456 when the cumulate time reaches 50% and the temperature difference reaches a steady state.

457 The inlet and outlet temperature difference of BHEs corresponding to the median time is
 458 used as another evaluation index to compare the heat transfer performance of BHEs under
 459 different modes. In cooling stage, the median of temperature difference is 2.34°C when the
 460 pumping-injection flow rate is $0 \text{ m}^3\cdot\text{d}^{-1}$. With the pumping-injection flow rate rises from 200
 461 $\text{m}^3\cdot\text{d}^{-1}$ to $1200 \text{ m}^3\cdot\text{d}^{-1}$, the growth rate of the median temperature difference varies from 11.5%
 462 to 73.9% . In heating stage, the median temperature difference is 1.76°C when BHEs run
 463 individually. With the pumping-injection flow rate increases from $200 \text{ m}^3\cdot\text{d}^{-1}$ to $1200 \text{ m}^3\cdot\text{d}^{-1}$, the
 464 growth rate of the median temperature difference increases from 10.2% to 34.1% . As the
 465 pumping-injection flow rate, Darcy velocity and the heat exchange intensity of BHEs all
 466 increase, thereby the decline rate of the temperature difference slows down while the time
 467 required reaching a steady state increase.

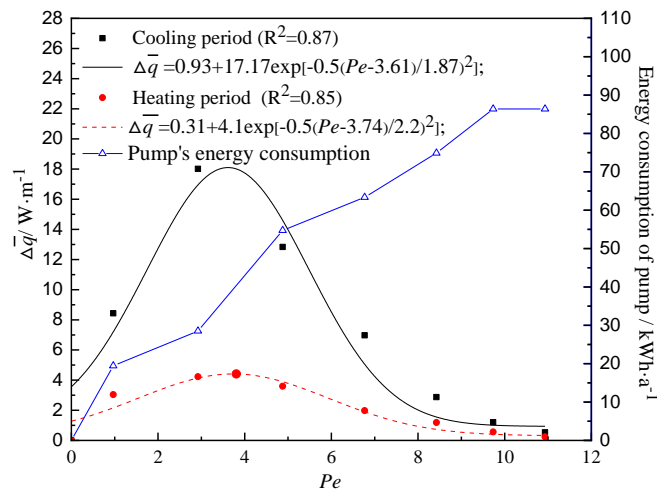
468 The heat transfer rates per unit borehole depth of BHEs (\bar{q}) rise gradually when
 469 pumping and injection flow rate increases (Figure 14). Taking the fifth year as an example,
 470 the \bar{q} in cooling and heating stages with the increase of the pumping-injection flow rate from
 471 $0 \text{ m}^3\cdot\text{d}^{-1}$ to $1200 \text{ m}^3\cdot\text{d}^{-1}$ varies from $30.3 \text{ W}\cdot\text{m}^{-1}$ and $25.4 \text{ W}\cdot\text{m}^{-1}$ to $82.2 \text{ W}\cdot\text{m}^{-1}$ and $39.6 \text{ W}\cdot\text{m}^{-1}$
 472 respectively.



473 **Figure 14.** Average heat transfer rates per unit borehole depth of BHEs ($\bar{q} = (\rho c_p M \Delta \bar{T}) / H$) in the fine
 474 sand layer over the whole operation period under different pumping-injection flow rate ΣG : (a) $\Sigma G = 0$
 475 $\text{m}^3 \cdot \text{d}^{-1}$; (b) $\Sigma G = 200 \text{ m}^3 \cdot \text{d}^{-1}$; (c) $\Sigma G = 400 \text{ m}^3 \cdot \text{d}^{-1}$; (d) $\Sigma G = 600 \text{ m}^3 \cdot \text{d}^{-1}$; (e) $\Sigma G = 800 \text{ m}^3 \cdot \text{d}^{-1}$; (f) $\Sigma G = 1200 \text{ m}^3 \cdot \text{d}^{-1}$

476 Thermal accumulation becomes serious with the continuous operation of the system,
 477 then the average heat transfer efficiency gets lower on the condition that the pumping and
 478 injection well ceases to work or the pumping-injection flow rate come to be smaller (200
 479 $\text{m}^3 \cdot \text{d}^{-1}$). As a result, cooling and heating quantity is declining every year. However, the
 480 rock-soil layer is not a single cold or heat source while an energy storage body has certain
 481 thermal storage and rejection. Therefore, thermal accumulation in the wells group's area
 482 enhances the heat storage capacity of the rock-soil layer across the season in the summer.
 483 During the heating stage, the temperature of the rock-soil layer is higher than the initial stage.

484 The temperature difference between the soil and the circulating solution increases so that the
 485 heat exchange quantity of the BHEs is improved at this stage.



486
 487 **Figure 15.** The total energy consumption of pumps and the increment of heat transfer rate per unit
 488 depth of BHEs ($\Delta \bar{q} = \bar{q}_{t+1} - \bar{q}_t$) change over Pe

489 Under the cooling and heating stages, the relation between $\Delta \bar{q}$ (known as the increment
 490 of average heat transfer rate per unit depth of BHEs) and Pe is determined by fitting which
 491 shows that $\Delta \bar{q}$ is distributed as a Gaussian function with the uptrend of Pe (Figure 15).
 492 Although the effect of convective heat transfer and thermal dispersion between BHEs and the
 493 rock-soil layer can be enhanced effectively by strengthening the velocity of groundwater
 494 seepage, the average heat transfer rates per unit borehole depth of BHEs \bar{q} does not raise
 495 linearly with the increase of the pumping-injection flow rate.

496 The research shows that Darcy velocity is only $0.6 \times 10^{-6} \sim 1.4 \times 10^{-6} \text{ m} \cdot \text{s}^{-1}$ when the pumping
 497 and injection flow rate is $400 \sim 600 \text{ m}^3 \cdot \text{d}^{-1}$, but the $\Delta \bar{q}$ respectively reaches $12.8 \sim 17.9 \text{ W} \cdot \text{m}^{-1}$ and
 498 $3.6 \sim 4.2 \text{ W} \cdot \text{m}^{-1}$ during the cooling stage and heating stage which are located on both sides of
 499 the extremum point of the distribution curve. As the designed Pumping-injection flow rate
 500 further increases, not only the $\Delta \bar{q}$ decreases gradually, but also the energy consumption of
 501 pumping and injection pumps increase that leads to the increase of operation cost of the
 502 system. Furthermore, the change of aquifer spatial structure will be irreversible if the forced
 503 seepage velocity is too high. Therefore, in order to obtain the best heat transfer enhancement
 504 effect, system environment and economic benefits, the pumping-injection flow rate when
 505 Darcy velocity reaches $0.6 \times 10^{-6} \sim 1.4 \times 10^{-6} \text{ m} \cdot \text{s}^{-1}$ is taken as the best reference range for CGSHP
 506 system, so the best flow rate range of pumping-injection wells is $400 \sim 600 \text{ m}^3 \cdot \text{d}^{-1}$ in this paper.

507 6. Conclusion

508 In this paper, CGSHP system is proposed as the same as the effect of the flow rate of
 509 pumping and injection wells on heat transfer characteristic of BHEs is studied for this system.
 510 The main conclusions of this study can be summarized as follows:

511 (a) For CGSHP system, an indoor sandbox is built by equation analysis method
 512 according to the principle of similarity criteria. At the same time, the equal volumetric weight
 513 by layered wet filling method is adopted to ensure that the porous medium in the sandbox is
 514 similar to that of the underground aquifer. So, the sandbox experiment could effectively
 515 reproduce the process of forced seepage and convection heat transfer in the aquifer. The

516 sandbox experiment and analytical model are used to verify the numerical simulation of
 517 FEFLOW7.1. The results show that the numerical simulation software FEFLOW7.1 can
 518 simulate effectively and correctly the evolution process of the aquifer temperature field
 519 during the taking heat of BHEs.

520 (b) When the pumping-injection flow rate from $200 \text{ m}^3\cdot\text{d}^{-1}$ to $1200 \text{ m}^3\cdot\text{d}^{-1}$, Darcy velocity
 521 in the fine sand layer increases approximately 10 times and the effect of convective heat
 522 transfer and thermal dispersion is enhanced. In the downstream region of BHEs, the thermal
 523 action radius is 2.6 times of the original radius. Hence, the cold and heat accumulation of
 524 CGSHP system can be alleviated effectively in the aquifer.

525 (c) For long-term running BHEs, the cumulative distribution curve of the inlet and outlet
 526 water average temperature difference is introduced to describe the duration of a certain heat
 527 exchange efficiency of BHEs. The average temperature difference corresponding to the
 528 median time is used as a new parameter for evaluating the heat transfer performance of BHEs.
 529 When the flow rate of pumping-injection wells increases, the average temperature difference
 530 and the average energy efficiency coefficient of BHEs as well as the heat exchange quantity of
 531 BHEs are improved substantially.

532 (d) In cooling and heating stages, the relation curve between the $\Delta \bar{q}$ and Pe has a
 533 Gaussian function distribution. Therefore, the heat exchange quantity of BHEs cannot be
 534 increased continuously by increasing the pumping-injection flow rate infinitely. The
 535 pumping-injection flow rate that can make Darcy velocity reaches $0.6 \times 10^{-6} \sim 1.4 \times 10^{-6} \text{ m}\cdot\text{s}^{-1}$ is the
 536 best reference range of CGSHP system, so the best pumping-injection flow rate is $400 \sim 600$
 537 $\text{m}^3\cdot\text{d}^{-1}$ in this paper.

538 (e) CGSHP system is proposed for the areas where the shallow-groundwater reserves
 539 are abundant but the seepage velocity is weak, such as the Bohai Plain in Tianjin, China. The
 540 results show that the system can control the seepage velocity of groundwater by changing the
 541 pumping-injection flow rate to enhance heat transfer, so CGSHP system has good
 542 controllability and predictability. In addition, CGSHP system should also be applicable to
 543 other countries with the same hydrogeological conditions as the region in this paper. The
 544 system has certain universality.

545 7. Declarations

546 **Author contributions:** JM and QJ performed conceptualization; JM and QJ performed data curation; JM
 547 and QJ performed formal analysis; JM and QJ provided methodology; QZ provided resources; YX and
 548 YW provided software simulation; FY validated data; QJ wrote the original draft; JM and QJ improved
 549 and revised the manuscript. All authors read and approved the final manuscript.

550 **Funding:** This research was funded by National Natural Science Foundation of China of Funder, grant
 551 number 41402228; This research was funded by Enterprise science and technology commissioner project
 552 of Tianjin of Funder, grant number 19JCTPJC48100.

553 **Availability of data and materials:** The datasets generated and analyzed during the current study are
 554 available from the corresponding author on reason-able request.

555 **Acknowledgments:** Thanks to the Tianjin Institute of Geotechnical Investigation Surveying for the
 556 hydrogeological parameters and relevant data provided.

557 **Conflicts of Interest:** The authors declare that they have no competing interests.

558 **Author details:** ¹School of Energy Safety Engineering, Tianjin Chengjian University, Tianjin 300384,
 559 China. ²Research Center for Efficient Utilization Technology of Geothermal Energy, Tianjin Chengjian
 560 University, Tianjin 300384, China.

561 Received: date Accepted: date

562 Published: date

563

564 References

- 565 1. National Development and Reform Commission. The 13th Five-Year Plan for the Exploitation and
566 Utilization of Geothermal Energy. N.D.R.C. Publishing: Beijing, China, 2017, Available online:
567 http://www.ndrc.gov.cn/zcfb/zcfbtz/201702/t20170204_837203.html. (in Chinese)
- 568 2. China Geological Survey. China Geothermal Energy Development Report. Beijing, China
569 Petrochemical Press: Beijing, China, 2018; pp.5-10. (in Chinese)
- 570 3. Richard A.B. Transient Heat Transfer in a U-tube Borehole Heat Exchanger. Applied Thermal
571 Engineering. 2014, 62, 256-266.
- 572 4. Richard A.B., Marvin D.S. Reference Data Sets for Vertical Borehole Ground Heat Exchanger
573 Models and Thermal Response Test Analysis. Geothermics. 2011, 40, 79-85.
- 574 5. A. Angelotti, L. Alberti. Energy Performance and Thermal Impact of a Borehole Heat Exchanger in
575 a sandy aquifer: Influence of the groundwater velocity. Energy Conversion and Management. 2014,
576 77, 700-708.
- 577 6. Jinzhong H. An Improved Analytical Model for Vertical Borehole Ground Heat Exchanger with
578 Multiple-Layer Substrates and Groundwater Flow. Applied Energy. 2017, 202, 537-549.
- 579 7. Jung C.C., Joonsang P. Numerical Evaluation of the Effects of Groundwater Flow on Borehole Heat
580 Exchanger Arrays. Renewable Energy. 2013, 52, 230-240.
- 581 8. Huajun W., Chengying Q. Thermal Performance of Borehole Heat Exchanger under Groundwater
582 Flow: A Case Study from Baoding. Energy and Buildings. 2009, 41, 1368-1373.
- 583 9. Alessandro C., Rajandrea S. Efficiency of Closed Loop Geothermal Heat Pumps: A Sensitivity
584 Analysis. Renewable Energy. 2014, 62, 737-746.
- 585 10. Yanling G., Xiaoli Z. 3D Dynamic Numerical Programming and Calculation of Vertical Buried Tube
586 Heat Exchanger Performance of Ground-Source Heat Pumps under Coupled Heat Transfer Inside
587 and Outside of Tube. Energy and Buildings. 2017, 139, 186-196.
- 588 11. Jozsef H.M., Michael d.P. Optimization of Energy Extraction for Vertical Closed-Loop Geothermal
589 Systems Considering Groundwater Flow. Energy Conversion and Management. 2013, 66, 1-10.
- 590 12. Chaofeng L., Peter J.C. Numerical Simulation of Ground Source Heat Pump Systems Considering
591 Unsaturated Soil Properties and Groundwater Flow Applied. Thermal Engineering. 2018, 139,
592 307-316.
- 593 13. Min L., Alvin C.K. Lai. Review of Analytical Models for Heat Transfer by Vertical Ground Heat
594 Exchangers (GHEs): A Perspective of Time and Space Scales. Applied Energy. 2015, 151, 178-191.
- 595 14. Matthew G.S., Darin W.N. A Ground Resistance for Vertical Bore Heat Exchangers with
596 Groundwater Flow. Energy Resources Technology-Transactions of the ASME. 2003, 125, 183-189.
- 597 15. Nairen D., Qinyun L. Heat Transfer in Ground Heat Exchangers with Groundwater Advection.
598 Thermal Sciences. 2004, 43, 1203-1211.
- 599 16. Nelson M.G., Peter B. Evaluating the Influence of Thermal Dispersion on Temperature Plumes from
600 Geothermal Systems Using Analytical Solutions. Thermal Sciences. 2011, 50, 1223-1231.
- 601 17. Nelson M.G., Philipp B. A Moving Finite Line Source Model to Simulate Borehole Heat Exchangers
602 with Groundwater Advection. Thermal Sciences. 2011, 50, 2506-2513.
- 603 18. Jin L., Joachim R. Review of Ground Investigations for Ground Source Heat Pump (GSHP) Systems.
604 Energy and Buildings. 2016, 117, 160-175.
- 605 19. A. Michopoulos, T. Zachariadis. Operation Characteristics and Experience of a Ground Source Heat
606 Pump System with a Vertical Ground Heat Exchanger. Energy. 2013, 51, 349-357.
- 607 20. Wonjun C., Ryoza O. Interpretation of Disturbed Data in Thermal Response Tests Using the Infinite
608 Line Source Model and Numerical Parameter estimation method. Applied Energy. 2015, 148,
609 476-488.
- 610 21. David C.S., A.C Elmore. The Observed Effects of Changes in Groundwater Flow on a Borehole Heat
611 Exchanger of a Large Scale Ground Coupled Heat pump system. Geothermics. 2018, 74, 240-246.
- 612 22. Ali S.S., Michel B. A Small-scale Experimental Apparatus to Study Heat Transfer in the Vicinity of
613 Geothermal Boreholes. HVAC&R Research. 2014, 20, 819-827.

- 614 23. Guozhu Z., Yimu G. Experimental Study on the Thermal Performance of Tunnel Lining GHE under
615 Groundwater Flow. *Applied Thermal Engineering*. 2016, 106, 784-795.
- 616 24. Linlin Z., Lei Z. Analyses on Soil Temperature Response to Intermittent Heat Rejection from BHEs
617 in Soils with Groundwater Advection. *Energy and Buildings*. 2015, 107, 355–365.
- 618 25. Selcuk E., Bertrand F. Multilayer Analytical Model for Vertical Ground Heat Exchanger with
619 Groundwater Flow. *Geothermics*. 2018, 71, 294-305.
- 620 26. Martin S., Jonathan D. Influence of Groundwater Flow on Cost Minimization of Ground Coupled
621 Heat Pump Systems. *Geothermics*. 2018, 73, 100-110.
- 622 27. Junye H., Gui L. The Hot Stack Performance of the Shallow Geothermal Heat Pump System
623 with/without Intensification State of Groundwater Seepage in Nanjing (China). *Energy and*
624 *Buildings*. 2017, 150, 558-566.
- 625 28. Wenke Z., Hongxing Y. The Research on Ring-coil Heat Transfer Models of Pile Foundation
626 Ground Heat Exchangers in the Case of Groundwater Seepage. *Energy and Buildings*. 2014, 71,
627 115-128.
- 628 29. Poul A.Ø., Neven D. Sustainable Development Using Renewable Energy Technology. *Renewable*
629 *Energy*. 2019, 146, 2430-2437.
- 630 30. Giti N., Younes N. Designing and Optimization of Solar Assisted Ground Source Heat Pump
631 System to Supply Heating, Cooling and Hot Water Demands. *Geothermics*. 2019, 82, 212–231.
- 632 31. H. Biglarian., M. H. Saidi. Economic and Environmental Assessment of
633 a Solar-assisted Ground Source Heat Pump System in a Heating-dominated Climate.
634 *Environmental Science and Technology*. 2019, 16, 3091-3098.
- 635 32. Zhijian L., Yuanwei L. Performance and Feasibility Study of Hybrid Ground Source Heat Pump
636 System Assisted with Cooling Tower for one Office Building Based on one Shanghai Case. *Energy*
637 *Conversion and Management*. 2018, 173, 28-37.
- 638 33. Xuemei G., Lei X. Investigation on the Optimal Cooling Tower Input Capacity of a Cooling Tower
639 Assisted Ground Source Heat Pump System. *Energy and Buildings*. 2018, 174, 239-253.
- 640 34. Rong M. Dealing with the spatial synthetic heterogeneity of aquifers in the north china plain: A case
641 study of Luancheng County in Hebei Province. Doctoral Dissertation, Chinese Academy of
642 Geological Sciences. Beijing, China, 2012. (in Chinese)
- 643 35. Zaiming Z. Spatial Variability and its Effect Mechanism of Soil Salinity in the Low Plain Around the
644 Bohai Sea. Doctoral Dissertation, Chinese Academy of Geological Sciences. Beijing, China, 2012. (in
645 Chinese)
- 646 36. Yujin N., Ryoza O. Development of a numerical model to predict heat exchange rates for a
647 ground-source heat pump system. *Energy and Buildings*. 2008.40:2133–2140.
- 648 37. Antonio C., Michele D.C. Investigations on the influence of aquifers on the ground temperature in
649 ground-source heat pump operation. *Applied Energy*. 2013.107: 35.
- 650 38. X. Mao, H. Prommer. Three-dimensional Model for Multi-component Reactive Transport with
651 Variable Density Groundwater flow. *Environmental Modelling & Software*. 2006, 21, 615-628.
- 652

Nomenclature	Λ	tensor of thermal hydrodynamic dispersion($W \cdot m^{-1} \cdot K^{-1}$)	
r	distance to the source /sink(m)	δ_{ij}	Kronecker tensor ($i=j, \delta_{ij} = 1; i \neq j, \delta_{ij} = 0$;))
t	time(s)	γ	compressibility coefficient
l	tube pitch of each BHE(m)	λ	thermal conductivity ($W \cdot m^{-1} \cdot K^{-1}$)
q	heat transfer rates per unit borehole depth of the BHEs ($W \cdot m^{-1}$)	α_L, α_T	longitudinal and transverse thermal dispersivity, respectively, of fluid (m)
H	borehole depth(m)	ρc	volumetric heat capacity ($J \cdot m^{-3} \cdot K^{-1}$)
T	temperature (K)	θ	dimensionless temperature
k	permeability(m^2)	Subscripts	
g	gravitational acceleration	x, y	longitudinal and transverse direction, respectively
Q_p	flow intensity of source (sink) term of flow field ($m^3 \cdot m^{-3} \cdot s^{-1}$)	r	refrigerant fluid
Q_T	heat intensity of heat source (sink) ($W \cdot m^{-3}$)	s	soil
x, y, z	Cartesian coordinates	f	fluid

u	absolute Darcy velocity(m·s ⁻¹)	s_0	initial state of rock soil layer
L	dimensionless distance	m	experimental system model
\bar{E}	the average heat transfer efficiency coefficient	i, o	pipe-in or internal, pipe-out or outer, respectively
\bar{Q}	actual average heat exchange quantity (J)	Superscripts	
\bar{Q}'	theoretical average heat exchange quantity (J)	cond	conduction
M	circulating flow flux of refrigerant (m ³ ·s ⁻¹)	disp	dispersion
Greek symbols			
μ	dynamic viscosity (Pa·s)		
ε	porosity		

653



© 2020 by the authors. Submitted for possible open access publication under the terms and conditions of the Creative Commons Attribution (CC BY) license (<http://creativecommons.org/licenses/by/4.0/>).

654